





# Deep-tissue SWIR imaging using rationally designed small red-shifted near-infrared fluorescent protein

Received: 6 June 2022

Accepted: 18 October 2022

Published online: 1 December 2022

 Check for updates

Olena S. Oliinyk<sup>1</sup>, Chenshuo Ma<sup>2</sup>, Sergei Pletnev<sup>3</sup>, Mikhail Baloban <sup>4</sup>, Carlos Taboada<sup>2</sup>, Huaxin Sheng<sup>5</sup>, Junjie Yao  & Vladislav V. Verkhusha <sup>1,4</sup> 

Applying rational design, we developed 17 kDa cyanobacteriochrome-based near-infrared (NIR-I) fluorescent protein, miRFP718nano. miRFP718nano efficiently binds endogenous biliverdin chromophore and brightly fluoresces in mammalian cells and tissues. miRFP718nano has maximal emission at 718 nm and an emission tail in the short-wave infrared (SWIR) region, allowing deep-penetrating off-peak fluorescence imaging *in vivo*. The miRFP718nano structure reveals the molecular basis of its red shift. We demonstrate superiority of miRFP718nano-enabled SWIR imaging over NIR-I imaging of microbes in the mouse digestive tract, mammalian cells injected into the mouse mammary gland and NF- $\kappa$ B activity in a mouse model of liver inflammation.

Biological tissues have strong optical attenuation in the visible wavelength range (350–700 nm), due to the absorption of hemoglobin and melanin, as well as the tissue scattering, which fundamentally limits the imaging depth of high-resolution optical technologies. By contrast, shifting the optical wavelengths to the near-infrared (NIR) range can substantially improve optical imaging at larger depths<sup>1,2</sup>. Recently, the second NIR window (NIR-II, 1,000–1,700 nm), the so-called short-wavelength infrared (SWIR) window, has gained tremendous interest by providing superior penetration depth, spatial resolution and image contrast in deep tissues, compared to the NIR-I window (700–1,000 nm)<sup>3–5</sup>. Thus, genetically encoded red-shifted NIR fluorescent proteins (FPs) are much needed for imaging applications<sup>6</sup>.

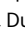
The state-of-the-art NIR FPs were engineered from bacterial phytochrome photoreceptors (BphPs)<sup>7</sup>. BphP-based FPs consist of PAS and GAF domains and have a relatively high molecular weight. We recently reported miRFP670nano protein, the first single-domain NIR FP developed from a GAF domain of cyanobacteriochrome (CBCR), and its improved variant miRFP670nano3 (refs. <sup>8,9</sup>). Compared to the BphP-derived NIR FPs, miRFP670nanos are twofold smaller,

naturally monomeric and have higher stability *in vitro* and in mammalian cells<sup>8,9</sup>.

To develop a small red-shifted NIR FP miRFP718nano, we applied a structure-based rational design to miRFP670nano, followed by directed molecular evolution (Supplementary Note 1 and Supplementary Figs. 1 and 2). We introduced point Cys mutation to bind biliverdin chromophore via its C3<sup>2</sup> atom. In such chromophore, the double bond between C2 and C3 atoms is preserved and is engaged in conjugation resulting in the red-shifted emission.

With excitation and emission maxima at 690 and 718 nm, miRFP718nano exhibited substantially red-shifted fluorescence and absorbance spectra compared to miRFP670nano (Fig. 1a–c and Supplementary Table 1). miRFP718nano has a long off-peak fluorescence emission tail that extends into the SWIR window. miRFP718nano fluorescence intensity above 1,000 nm was threefold higher compared to miRFP670nano and about two- and 1.5-fold higher than that of miRFP703 and miRFP709, respectively (Fig. 1d and Supplementary Table 1). Thus, the spectral properties of miRFP718nano make it a highly promising probe for SWIR imaging.

<sup>1</sup>Medicum, Faculty of Medicine, University of Helsinki, Helsinki, Finland. <sup>2</sup>Department of Biomedical Engineering, School of Engineering, Duke University, Durham, NC, USA. <sup>3</sup>Vaccine Research Center, National Institute of Allergy and Infectious Diseases, National Institutes of Health, Bethesda, MD, USA.

<sup>4</sup>Department of Genetics and Gruss-Lipper Biophotonics Center, Albert Einstein College of Medicine, Bronx, NY, USA. <sup>5</sup>Department of Anesthesiology, School of Medicine, Duke University, Durham, NC, USA.  e-mail: [junjie.yao@duke.edu](mailto:junjie.yao@duke.edu); [vladislav.verkhusha@einsteinmed.edu](mailto:vladislav.verkhusha@einsteinmed.edu)

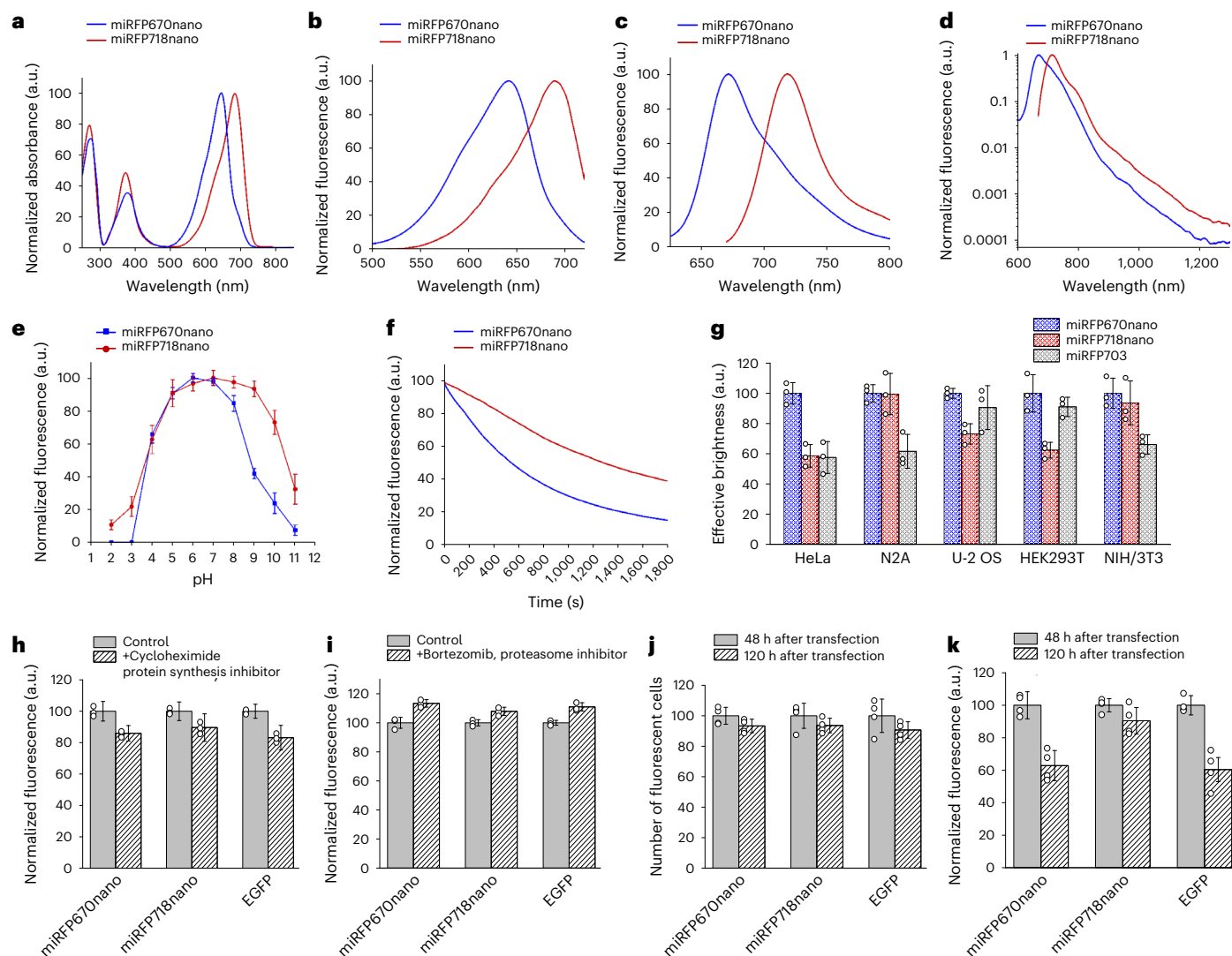


**Fig. 1 | Properties of red-shifted miRFP718nano in comparison with parental miRFP670nano.** **a**, Absorbance spectra. **b**, Fluorescence excitation spectra (emission at 740 nm). **c, d**, Fluorescence emission spectra in the linear (**c**) and in the logarithmic (**d**) scales (excitation at 580 nm for miRFP670nano and 650 nm for miRFP718nano). **e**, pH dependencies of NIR fluorescence. Data are presented as mean values  $\pm$  s.d. for  $n = 3$  experiments. In **a–d**, spectroscopic measurements were performed in PBS. **f**, Photobleaching in live HeLa cells with 665/45 nm excitation filter. Light power density at the back aperture of the objective lens was  $8.25 \text{ mW cm}^{-2}$ , resulting in  $4.3 \text{ W cm}^{-2}$  at the focal objective plane. Cells were incubated in a live-cell imaging solution. **g**, Cellular brightness of miRFP718nano, miRFP670nano and miRFP703 in live mammalian cells. Fluorescence was analyzed 72 h after transfection. The effective brightness of miRFP670nano was assumed to be 100% for each cell type. NIR fluorescence intensity was normalized to the excitation efficiency of each NIR FP by 640 nm laser, and to the emission spectrum of each FP in the emission filter. Gating was performed

as shown in Supplementary Fig. 3. **h**, Mean fluorescence intensity of HeLa cells transiently transfected with miRFP718nano, miRFP670nano and EGFP before and after 4 h of incubation with a protein synthesis inhibitor cycloheximide ( $20 \mu\text{g ml}^{-1}$ ). Fluorescence was normalized to control conditions. **i**, Mean fluorescence intensity of HeLa cells transiently transfected with miRFP718nano, miRFP670nano and EGFP before and after 4 h of incubation with an inhibitor of proteasome-dependent protein degradation bortezomib ( $10 \mu\text{M}$ ). Fluorescence was normalized to control conditions. In **g**, **h** and **i** data are presented as mean values  $\pm$  s.d. for  $n = 3$  transfection experiments. **j**, Mean fluorescence intensity of live HeLa cells transiently transfected with miRFP718nano, miRFP670nano and EGFP 48 and 120 h after transfection normalized to that at 48 h. **k**, Number of FP expressing (fluorescent) HeLa cells transiently transfected with parental miRFP670nano, miRFP718nano or EGFP was calculated at 48 and 120 h after transfection and normalized to that at 48 h. In **j** and **k**, data are presented as mean values  $\pm$  s.d. for  $n = 4$  transfection experiments. a.u., arbitrary units.

The fluorescence of miRFP718nano was stable over a wide pH range of 4.0–10.0. (Fig. 1e). miRFP718nano exhibited improved photostability, which was 2.3-fold higher than that of miRFP670nano and several-fold higher than the photostability of BphP-derived NIR FPs (Fig. 1f and Supplementary Table 1)<sup>10,11</sup>.

In transiently transfected HeLa, N2a, U-2 OS, human embryonic kidney 293T (HEK293T) and NIH/3T3 cells, expressing miRFP670nano, miRFP718nano and miRFP703, miRFP718nano outperformed BphP-derived miRFP709 by 1.3-fold and has brightness comparable

with that of spectrally close miRFP703 (Fig. 1g, Supplementary Fig. 3 and Supplementary Table 1). In addition to cell lines, primary cortical rat neurons transfected with miRFP718nano exhibited bright fluorescence (Supplementary Fig. 4).

The protein stability tests with cycloheximide, an inhibitor of translational elongation, and with bortezomib, an inhibitor of proteasome-dependent protein degradation, both showed that miRFP718nano similar to enhanced green fluorescent protein (EGFP) and miRFP670nano is highly stable in mammalian cells (Fig. 1h,i).

The comparison of brightness and percentage of fluorescent cells 48 and 120 h after transfection further confirmed that miRFP718nano had high protein stability (Fig. 1j,k). Similar to the miRFP670nano, in transiently transfected HeLa cells miRFP718nano fluorescence reached a maximum at 72 h after transfection (Supplementary Fig. 5).

miRFP718nano performed well as a fluorescent probe in various N- and C-terminal, as well as internally labeled fusion proteins (Supplementary Fig. 6). Coexpression of the miRFP670nano and miRFP718nano fusions, enabled the clear separation of miRFP670nano and miRFP718 fluorescence signals for two-color NIR imaging (Supplementary Fig. 7).

We calculated that the Förster radius for the miRFP670nano–miRFP718nano fluorescence resonance energy transfer (FRET) pair is 7.9 nm. Further evaluation of miRFP718nano as a FRET acceptor for miRFP670nano in a biosensor for c-Jun N-terminal kinase (JNK) activity<sup>12</sup> (Supplementary Fig. 8a) showed that miRFP670nano and miRFP718nano formed an efficient NIR FRET pair (Supplementary Fig. 8b,c), which, similarly to BphP-based NIR FPs<sup>6,13–16</sup>, can be used to engineer various fully NIR biosensors.

To gain insights into the structural basis of the miRFP718nano properties, we determined its crystal structure at 1.7 Å resolution (Extended Data Fig. 1, Supplementary Note 2 and Supplementary Tables 1 and 2). The root mean square deviation between miRFP718nano and miRFP670nano<sup>8</sup> superimposed by C<sup>α</sup> atoms does not exceed 0.74 Å. Both proteins have a similar GAF fold with the N and C termini positioned close to each other (Extended Data Fig. 1a,b,d,e,g). This fold is similar to that of the GAF domains of BphP-based miRFP709 linked to the adjacent PAS domain (Extended Data Fig. 1c,f)<sup>17</sup>.

The crystal structure of miRFP718nano showed that its chromophore forms a covalent thioether bond between the C3<sup>2</sup> atom of biliverdin ring A and the rationally introduced Cys57 (Extended Data Fig. 1b,e,j). In contrast, the biliverdin chromophore of miRFP670nano is connected to the conserved Cys86 by the C3<sup>1</sup> atom (Extended Data Fig. 1a,d,k). The biliverdin chromophore of miRFP718nano also has a chemical structure, featuring a double bond between C2 and C3 atoms, absent in parental miRFP670nano<sup>8</sup>, thus extending the chromophore conjugation system. This chromophore was never observed before in CBCR-derived NIR FPs.

To demonstrate SWIR imaging's advantages over NIR-I imaging<sup>4,18–20</sup>, we first characterized miRFP718nano's SWIR performance on bacteria in phantoms (Supplementary Fig. 9). NIR-I (750/40 nm emission) and SWIR (1050 nm long-pass emission) imaging were individually performed with the same excitation at 660 nm. SWIR imaging could better maintain the spatial resolution and image contrast in a scattering medium (Supplementary Fig. 10).

We then validated *in vivo* performance of miRFP718nano-enabled SWIR imaging by tracking miRFP718nano-expressing bacteria motility in the mouse digestion model<sup>21</sup>. Both NIR-I and SWIR images showed the migration of the bacteria (Supplementary Fig. 11a), but NIR-I images were blurred. By contrast, SWIR images had much more confined signals inside the stomach and along the intestine (Supplementary Fig. 11b). We observed an approximately 3-cm-long migration path within 60 min, consistent with previous reports<sup>22,23</sup>.

We next evaluated SWIR imaging in mammalian cells, including miRFP670nano- and miRFP718nano-expressing HEK293T cells. Whereas both cell types had similar NIR-I fluorescence levels, miRFP718nano-expressing cells had twofold stronger SWIR fluorescence (Supplementary Fig. 12a). In NIR-I images, the spatial resolution degraded from 0.1 mm at 0-mm depth to 1.14 mm at 3-mm depth and 1.96 mm at 5-mm depth (Supplementary Fig. 12b). By contrast, in SWIR images, the spatial resolution was 0.4 mm at 3-mm depth and 0.8 mm at 5-mm depth, approximately 65 and 61% better than NIR-I images (Supplementary Fig. 12c).

Next, we compared miRFP718nano- and miRFP670nano3-expressing HEK293T cells (Supplementary Fig. 13a–c). miRFP718nano-expressing cells had 2.3-fold stronger SWIR signals than miRFP670nano3-expressing cells, as well as higher image contrast and less scattering-induced blurring (Supplementary Fig. 13a). We have quantified SWIR and NIR-I emission ratio (Supplementary Fig. 13d). miRFP718 has the highest SWIR/NIR-I emission ratio, which is more than threefold as large as that of miRFP670nano and miRFP670nano3.

We next injected miRFP718nano- or miRFP670nano-expressing HEK293T cells into the mouse mammary glands at roughly 1.5 mm depth (Supplementary Fig. 14a,b). SWIR imaging had better detection sensitivity than NIR-I imaging for both types of cell (Supplementary Fig. 14c). We increased the exposure time for low cell numbers, which benefited SWIR imaging but not NIR-I imaging due to the strong NIR-I autofluorescence (Supplementary Fig. 14a,b). SWIR imaging of miRFP718nano-expressing HEK293T cells had the highest sensitivity under all conditions (Supplementary Fig. 14d). Even with the lowest cell number of  $1 \times 10^4$ , SWIR image of miRFP718nano-expressing cells had a signal-to-background ratio of roughly 3.7, which was three times better than NIR-I image.

To validate miRFP718nano for monitoring signaling pathways *in vivo*, we engineered a miRFP718nano-based nuclear factor-κB (NF-κB) transcription reporter, a key regulator of inflammatory responses. After activation NF-κB binds to the consensus sequence on DNA (NF-κB response element)<sup>24</sup>. We constructed the inflammation reporter containing five copies of an NF-κB response element that drives the miRFP718nano transcription on NF-κB activation (Fig. 2a).

To study the efficiency of the engineered NF-κB reporter, we transiently transfected HEK293T cells with a miRFP718nano-based reporter. Nonstimulated cells showed weak or no miRFP718nano expression (Fig. 2b, bottom), indicating a low background activity. In contrast, cells stimulated with 20 ng ml<sup>-1</sup> tumor necrosis factor-α (TNF-α) demonstrated strong miRFP718nano fluorescence (Fig. 2b,c). Stimulation of cells with different amounts of TNF-α showed that 5 ng ml<sup>-1</sup> TNF-α was sufficient to fully activate the reporter while 1 ng ml<sup>-1</sup> TNF-α caused more than 50% of activation (Fig. 2d).

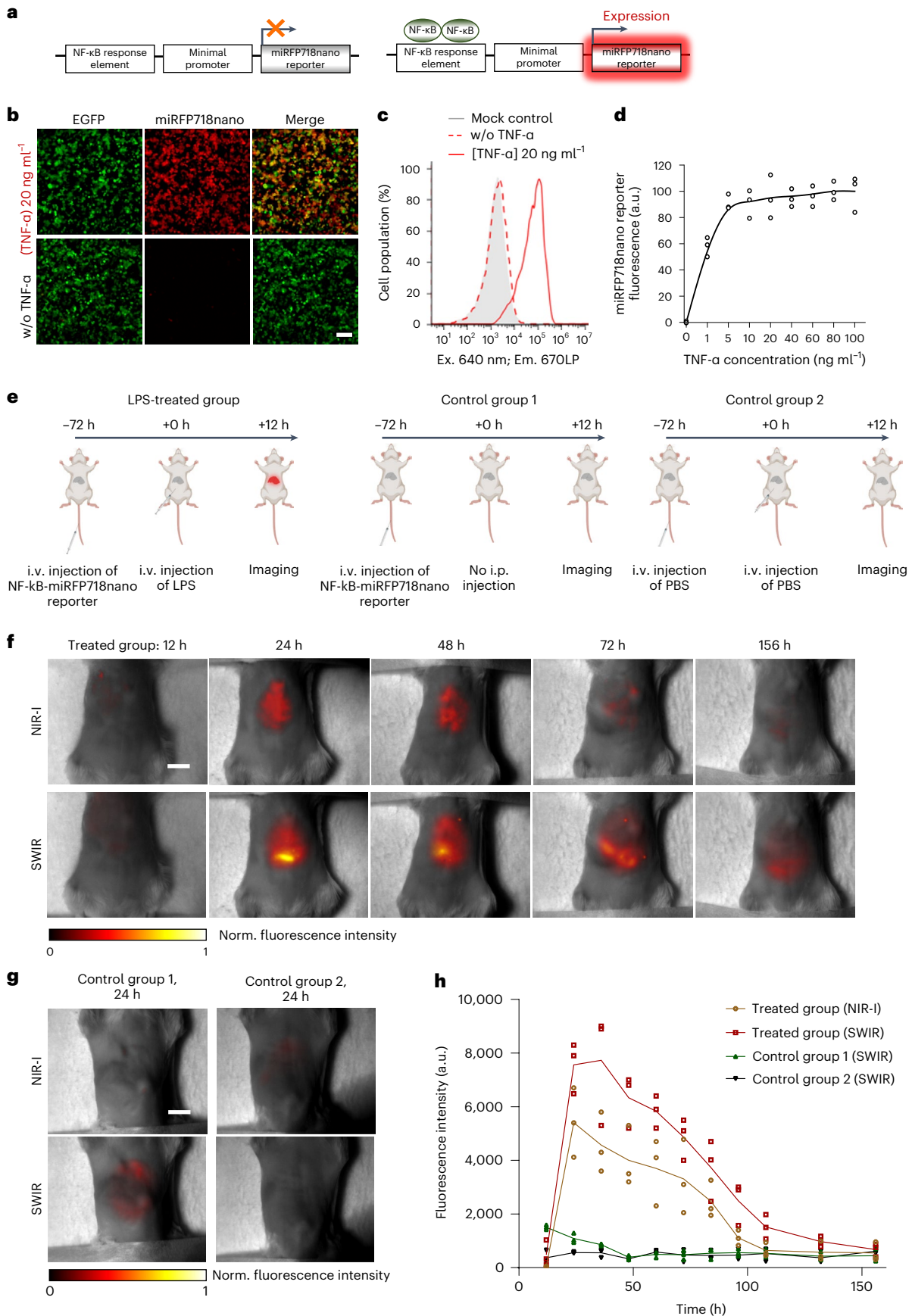
To monitor the NF-κB activity *in vivo*, we adapted a gene delivery approach in the liver based on hydrodynamic transfection<sup>25</sup>. After 72 h, we induced acute inflammation with an intraperitoneal injection of *Escherichia coli* lipopolysaccharide (LPS). The first control group received NF-κB-based miRFP718nano reporter plasmid through the tail vein but did not receive an LPS injection. The second control group received two injections of phosphate-buffered saline (PBS) instead of the reporter plasmid and LPS (Fig. 2e). For the LPS-treated group,

**Fig. 2 | miRFP718nano as a reporter of inflammation.** **a**, Schematic representation of miRFP718nano-based reporter of inflammation. **b**, HEK293T cells transfected with the miRFP718nano-based reporter of inflammation and cotransfected with pEGFP-N1 (1:10), 20 h after stimulation with TNF-α (20 ng ml<sup>-1</sup>) (top row) or nontreated (w/o, bottom row). For imaging of miRFP718nano and EGFP, 685/20 nm excitation (Ex.) and 725/40 nm emission (Em.), and 485/20 nm excitation and 525/30 nm emission filters were used, respectively. Representative images of two experiments are shown. Scale bar, 100 μm. **c**, Mean fluorescence intensity of HEK293T cells transiently transfected with miRFP718nano reporter of inflammation 20 h after stimulation with TNF-α (20 ng ml<sup>-1</sup>). Gating was performed as shown in Supplementary Fig. 3. **d**, TNF-α dose-response in

HEK293T cell transfected with miRFP718nano reporter of inflammation, measured by flow cytometry. Data are presented as mean values ± s.d. for  $n = 3$  transfection experiments. **e**, The schematics of developing the mouse model injected with miRFP718nano reporter plasmid and LPS, as well as the two control models with only the plasmid or only PBS. i.v., intravenous; i.p., intraperitoneal. **f**, Representative NIR-I and SWIR images of the LPS-treated group at different time points after the LPS injection. Norm., normalized. Scale bar, 10 mm. **g**, Representative NIR-I and SWIR images of the two control groups at 24 h. **h**, The time course of NIR-I and SWIR signals in the liver region of the three animal groups ( $n = 3$  for each group).

in vivo results showed clear fluorescence of miRFP718nano in the liver, which peaked at 24 h after the LPS injection, in both NIR-I and SWIR images (Fig. 2f). No significant fluorescence emission was observed

in the two control groups (Fig. 2g and Supplementary Fig. 15). The fluorescence signals gradually decreased over 6.5 days, reflecting the progress of LPS-induced inflammation (Fig. 2h). As expected, SWIR



images provided stronger signals as well as better contrast (Supplementary Fig. 16). Moreover, SWIR images were able to detect weak NF- $\kappa$ B activity at the late stages of the inflammation.

In conclusion, using a structure-based design followed by directed molecular evolution, we have developed a 17 kDa red-shifted NIR FP, miRFP718nano. miRFP718nano brightly fluoresces in both NIR-I and SWIR windows without supply of exogenous biliverdin chromophore, has high protein stability and performs well in terminal and internal protein tags. Spectral properties of miRFP718nano enable its use as a FRET acceptor for blue-shifted 17 kDa miRFP670nano, resulting in the smallest fully NIR FRET pair. The structure of miRFP718nano and its biliverdin chromophore revealed the basis of its red shift and explained the effect of rational design. This rational design could be further applied to other CBCRs. CBCRs demonstrate a large spectral diversity and among them, CBCRs with native red-shifted fluorescence are of particular interest<sup>7,26</sup>. Further efforts directed at the discovery of more red-shifted CBCRs and applying described strategy should result in NIR FPs with substantially SWIR-shifted fluorescence.

Comparison of miRFP718nano in the NIR-I and SWIR range demonstrated its superior performance in the SWIR window, such as larger penetration depth, higher spatial resolution and contrast, and improved detection sensitivity. We showed miRFP718nano-based SWIR imaging on several animal models. More generally, we demonstrated that the long off-peak fluorescence emission tail of red-shifted NIR FP enables advanced SWIR deep-tissue imaging. Unlike in the NIR-I window, biological tissues have relatively weak autofluorescence and optical scattering in the SWIR window, and thus increasing the exposure time can improve the image contrast without strong background signals or blurring the targets. Compared with NIR fluorescent dyes, miRFP718nano can be specifically expressed in tissues through genetic encoding, does not need complex exogenous delivery, and has high biocompatibility for longitudinal studies.

## Online content

Any methods, additional references, Nature Portfolio reporting summaries, source data, extended data, supplementary information, acknowledgements, peer review information; details of author contributions and competing interests; and statements of data and code availability are available at <https://doi.org/10.1038/s41592-022-01683-0>.

## References

- Frangioni, J. V. In vivo near-infrared fluorescence imaging. *Curr. Opin. Chem. Biol.* **7**, 626–634 (2003).
- Scholkmann, F. et al. A review on continuous wave functional near-infrared spectroscopy and imaging instrumentation and methodology. *Neuroimage* **85**, 6–27 (2014).
- Welsher, K. et al. A route to brightly fluorescent carbon nanotubes for near-infrared imaging in mice. *Nat. Nanotechnol.* **4**, 773–780 (2009).
- Smith, A. M., Mancini, M. C. & Nie, S. Bioimaging: second window for in vivo imaging. *Nat. Nanotechnol.* **4**, 710–711 (2009).
- Feng, Z. et al. Perfecting and extending the near-infrared imaging window. *Light Sci. Appl.* **10**, 197 (2021).
- Shcherbakova, D. M., Stepanenko, O. V., Turoverov, K. K. & Verkhusha, V. V. Near-infrared fluorescent proteins: multiplexing and optogenetics across scales. *Trends Biotechnol.* **36**, 1230–1243 (2018).
- Oliinyk, O. S., Chernov, K. G. & Verkhusha, V. V. Bacterial phytochromes, cyanobacteriochromes and allophycocyanins as a source of near-infrared fluorescent probes. *Int. J. Mol. Sci.* **18**, 1691 (2017).
- Oliinyk, O. S., Shemetov, A. A., Pletnev, S., Shcherbakova, D. M. & Verkhusha, V. V. Smallest near-infrared fluorescent protein evolved from cyanobacteriochrome as versatile tag for spectral multiplexing. *Nat. Commun.* **10**, 279 (2019).
- Oliinyk, O. S. et al. Single-domain near-infrared protein provides a scaffold for antigen-dependent fluorescent nanobodies. *Nat. Methods* **19**, 740–750 (2022).
- Shcherbakova, D. M. et al. Bright monomeric near-infrared fluorescent proteins as tags and biosensors for multiscale imaging. *Nat. Commun.* **7**, 12405 (2016).
- Yu, D. et al. A naturally monomeric infrared fluorescent protein for protein labeling in vivo. *Nat. Methods* **12**, 763–765 (2015).
- Komatsu, N. et al. Development of an optimized backbone of FRET biosensors for kinases and GTPases. *Mol. Biol. Cell* **22**, 4647–4656 (2011).
- Shcherbakova, D. M. Near-infrared and far-red genetically encoded indicators of neuronal activity. *J. Neurosci. Methods* **362**, 109314 (2021).
- Shcherbakova, D. M., Cox Cammer, N., Huisman, T. M., Verkhusha, V. V. & Hodgson, L. Direct multiplex imaging and optogenetics of Rho GTPases enabled by near-infrared FRET. *Nat. Chem. Biol.* **14**, 591–600 (2018).
- Li, L., Hsu, H. C., Verkhusha, V. V., Wang, L. V. & Shcherbakova, D. M. Multiscale photoacoustic tomography of a genetically encoded near-infrared FRET biosensor. *Adv. Sci.* **8**, e2102474 (2021).
- Shemetov, A. A. et al. A near-infrared genetically encoded calcium indicator for in vivo imaging. *Nat. Biotechnol.* **39**, 368–377 (2021).
- Baloban, M. et al. Designing brighter near-infrared fluorescent proteins: insights from structural and biochemical studies. *Chem. Sci.* **8**, 4546–4557 (2017).
- Chang, B. et al. A phosphorescent probe for in vivo imaging in the second near-infrared window. *Nat. Biomed. Eng.* **6**, 629–639 (2021).
- Jeong, S. et al. Multiplexed in vivo imaging using size-controlled quantum dots in the second near-infrared window. *Adv. Healthc. Mater.* **7**, e1800695 (2018).
- Robinson, J. T. et al. In vivo fluorescence imaging in the second near-infrared window with long circulating carbon nanotubes capable of ultrahigh tumor uptake. *J. Am. Chem. Soc.* **134**, 10664–10669 (2012).
- Hugenholtz, F. & de Vos, W. M. Mouse models for human intestinal microbiota research: a critical evaluation. *Cell. Mol. Life Sci.* **75**, 149–160 (2018).
- Hamano, N., Inada, T., Iwata, R., Asai, T. & Shingu, K. The  $\alpha$ 2-adrenergic receptor antagonist yohimbine improves endotoxin-induced inhibition of gastrointestinal motility in mice. *Br. J. Anaesth.* **98**, 484–490 (2007).
- Wang, D. et al. Trans-illumination intestine projection imaging of intestinal motility in mice. *Nat. Commun.* **12**, 1682 (2021).
- Liu, T., Zhang, L., Joo, D. & Sun, S. C. NF- $\kappa$ B signaling in inflammation. *Signal Transduct. Target Ther.* **2**, 17023 (2017).
- Osorio, F. G., de la Rosa, J. & Freije, J. M. Luminescence-based in vivo monitoring of NF- $\kappa$ B activity through a gene delivery approach. *Cell Commun. Signal* **11**, 19 (2013).
- Fushimi, K. & Narikawa, R. Phytochromes and cyanobacteriochromes: photoreceptor molecules incorporating a linear tetrapyrrole chromophore. *Adv. Exp. Med Biol.* **1293**, 167–187 (2021).

**Publisher's note** Springer Nature remains neutral with regard to jurisdictional claims in published maps and institutional affiliations.

Springer Nature or its licensor (e.g. a society or other partner) holds exclusive rights to this article under a publishing agreement with the author(s) or other rightsholder(s); author self-archiving of the accepted manuscript version of this article is solely governed by the terms of such publishing agreement and applicable law.

© The Author(s), under exclusive licence to Springer Nature America, Inc. 2022, corrected publication 2023

## Methods

### Mutagenesis and directed molecular evolution

Genes encoding miRFP670nano, miRFP718nano and their mutants were cloned into a pBAD/His-B vector (Thermo-Fisher Scientific) by using the KpnI and EcoRI restriction sites. All oligonucleotide primers for PCR amplification and saturated mutagenesis were purchased from Biomers (Supplementary Table 4). LMG194 (Invitrogen/Thermo-Fisher Scientific) was used as host *E. coli* cells. For biliverdin productions LMG194 was transformed with a pWA23h plasmid encoding heme oxygenase from *Bradyrhizobium ORS278* under rhamnose promoter<sup>10</sup>. Random mutagenesis was performed with a GeneMorph II random mutagenesis kit (Agilent Technologies). Saturated and site-specific mutageneses were performed by overlap-extension PCR. Resulted mixtures of mutated genes were cloned into pBAD/His-B vector and electroporated into LMG194 cells, transformed with a pWA23h plasmid. Bacterial libraries of mutants contained  $10^7$ – $10^8$  clones. FACS-screening of mutant libraries was performed with an Influx cell sorter (BD Biosciences), using a 640 nm excitation laser and 725/40 nm emission filter. For sorting, the bacteria were grown in a Luria-Bertani medium, containing carbenicillin and kanamycin ( $100 \mu\text{g ml}^{-1}$ , Thermo-Fisher Scientific) and supplemented with 0.02% rhamnose (Santa Cruz) and 0.005% arabinose (Calbiochem) for 5 h at 37 °C and then overnight at 22 °C. Before sorting bacterial cells were pelleted, washed and diluted with ice-cold PBS to an optical density of 0.03 at 600 nm. The brightest collected bacterial cells were incubated in SOC medium for 1 h at 37 °C and then plated on LB-ampicillin-kanamycin Petri dishes supplemented with 0.005% arabinose and 0.02% rhamnose overnight at 37 °C. Screening of the brightest clones was performed with a Leica M205 fluorescence stereomicroscope equipped with a CCD camera (Tucsen), using 700/20 nm excitation and 730 nm long-pass emission filters (Chroma). To exclude blue-shifted mutants, 615/30 nm excitation and 670/30 nm emission filters (Chroma) were used. The fluorescence spectra of selected clones were then measured using a Cary Eclipse fluorimeter (Agilent Technologies) and around 30 brightest red-shifted clones were subcloned into a pcDNA3.1 plasmid (Invitrogen/Thermo-Fisher Scientific) and tested in transiently transfected HeLa cells.

### Protein expression and characterization

Proteins were expressed in LMG194 bacterial cells, cotransformed with pWA23h plasmid, as described above for sorting of libraries of mutants. Protein purification was performed with Ni-NTA agarose (Qiagen). For elution, PBS containing 100 mM EDTA was used.

For the recording of fluorescence spectra, the Cary Eclipse fluorimeter (Agilent Technologies) was used. Absorbance spectra were recorded with a Hitachi U-2000 spectrophotometer. The extinction coefficient of miRFP718nano was determined as a ratio between the maximum absorbance of the main peak at the Q band and the side peak at the Soret band assuming that the extinction coefficient at the Soret band corresponds to  $39,900 \text{ M}^{-1} \text{ cm}^{-1}$  (ref. <sup>10</sup>). The fluorescence quantum yield of miRFP718nano was determined using miRFP709 as standard. The pH stability was studied using a series of Hydriion buffers (Micro Essential Laboratory). Data fitting and statistical analysis were performed using OriginPro 2021b v.9.8.5.212 (OriginLab) and Excel v.15.36 (Microsoft) software.

### Protein crystallization

For crystallization, miRFP718nano was equilibrated in 20 mM Tris-HCl, 300 mM NaCl at pH 8.0 buffer and concentrated to  $27.8 \text{ mg ml}^{-1}$ . Initial crystallization conditions were found with the NT8 crystallization robot (Formulatrix) using Hampton Research, Jena Bioscience and Molecular Dimensions screens. The conditions were further optimized with additive screens. The best crystals could be obtained from 12.6% PEG 6000, 0.1 M lithium sulfate, 0.07 M citric acid buffer pH 3.5 and 2.1% D-sorbitol. The crystals suitable for X-ray data collection were grown by the hanging-drop vapor diffusion method. In the large-scale

crystallization experiment, 2  $\mu\text{l}$  of the protein solution was mixed with 2  $\mu\text{l}$  of the reservoir solution and incubated against 500  $\mu\text{l}$  of the same reservoir solution at 20 °C for 1 week.

### Determination of protein structure

X-ray data were acquired on SER-CAT 22-ID and 22-BM beamline stations (Advanced Photon Source, Argonne National Laboratory). Before data collection, the crystals were flash-frozen in a 100 K nitrogen gas stream. Diffraction images were processed with HKL2000 (ref. <sup>27</sup>). The statistics and data processing are given in Supplementary Table 2. The structure was solved by the molecular replacement method with MOLREP v.11.0 (ref. <sup>28</sup>) using the structure of miRFP670nano (Protein Data Bank (PDB) ID 6MGH) as a search model. To remove model bias, the structure was rebuilt with ARP/wARP model building and density improvement software<sup>29</sup>. The structure refinement was carried out with REFMAC5 (ref. <sup>30</sup>) (CCP4 suite) v.8.0.005 and PHENIX.REFINE<sup>31</sup> (PHENIX suite) v.1.8.4-1496 programs. A realspace model correction and structure validation were performed with COOT v.0.9.8.1 (ref. <sup>32</sup>). The refinement statistics are given in Supplementary Table 3.

### Construction of mammalian plasmids

To construct plasmids encoding miRFP718nano or its mutants, the respective genes were cloned into the pcDNA3.1 plasmid (Invitrogen/Thermo-Fisher Scientific) by using the KpnI and EcoRI restriction sites.

To engineer plasmids for protein tagging and labeling of intracellular structures, the gene encoding miRFP718nano was swapped with the gene encoding miRFP670nano either as C- (for  $\alpha$ -tubulin, actin, myosin and vesicular protein clathrin), N-terminal fusions (for lysosomal membrane glycoprotein LAMP1, mitochondria, histone H2B) or internal fusions (for  $\beta$ 2 adrenergic receptor and G-protein  $\alpha$  subunit). To engineer a JNK activity NIR-biosensor plasmids, a gene encoding miRFP720 was replaced with the gene encoding miRFP718nano by NotI/XbaI sites in the reported previously NIR FRET biosensors of JNK kinase<sup>8</sup>. To construct a miRFP718nano-based reporter of inflammation, the gene encoding miRFP718nano was swapped with a gene encoding NLucP in the pNL3.2.NF- $\kappa$ B-RE[NLucP/NF- $\kappa$ B-RE/Hygro] vector (Promega).

### Mammalian cells and transfection

HeLa (CCL-2), N2A (CCL-131), U-2 OS (HTB-96), HEK293T (CRL-3216) and NIH3T3 (CRL-1658) cells were obtained from the ATCC. Cells were cultured in a DMEM medium supplemented with 10% FBS, 0.5% penicillin-streptomycin and 2 mM glutamine (Invitrogen/Thermo-Fisher Scientific) at 37 °C in a humidified 5% CO<sub>2</sub> atmosphere. For fluorescence microscopy, cells were plated in 35 mm glass-bottom Petri dishes (Greiner Bio-One International). Transient transfections were performed using polyethylenimine<sup>33</sup>.

### Neuronal culture and transfection

Primary embryonic rat cortical neurons were prepared in the Neuronal Cell Culture Unit of the University of Helsinki. The embryos staged at E17–18 from the female rats were used. Animals were kept in standard conditions. All animal work was performed under the ethical guidelines of the European convention and regulations of the Ethics Committee for Animal Research of the University of Helsinki. Cells were plated at a density of 500,000–700,000 per 35 mm glass-bottom dish, coated with poly-L-lysine ( $0.01 \text{ mg ml}^{-1}$ ) (Merck). Neurons were grown at 37 °C and 5% CO<sub>2</sub> in a neurobasal medium (Gibco) supplemented with B27 (Invitrogen/Thermo-Fisher Scientific), L-glutamine (Invitrogen/Thermo-Fisher Scientific) and penicillin-streptomycin (Lonza). Cultured neurons were transfected with pcDNA plasmids encoding miRFP718nano at 4–5 days in vitro (DIV) using Effectene Transfection Reagent (Qiagen) and imaged 48 h after transfection.

### NF- $\kappa$ B-based transcription reporter of inflammation

HEK293T cells were transfected with plasmids encoding reporter of inflammation and EGFP (1:10) and stimulated with TNF- $\alpha$  in indicated concentrations. Measurement of miRFP718nano fluorescence was performed by flow cytometry and fluorescent microscopy 20 h after stimulation.

### Wide-field fluorescence microscopy

Live cells were imaged with an Olympus IX81 inverted epifluorescence microscope equipped with a Xenon lamp (Lambda LS, Sutter),  $\times 60$  1.35 NA oil objective lens (UPlanSApo, Olympus) and an ORCA-Flash4.0 V3 camera (Hamamatsu). During imaging, HeLa cells were incubated in a cell imaging solution (Life Technologies-Invitrogen) and kept at 37 °C. Neurons were imaged in cultured media. The microscope was operated with a SlideBook v.6.0.8 software (Intelligent Imaging Innovations).

To separately image miRFP670nano and miRFP18nano, two filter sets (605/30 nm exciter with 667/30 nm emitter, and 685/20 nm exciter with 725/40 nm emitter) (Chroma) were used. For imaging of miRFP718nano 685/20 nm excitation and 725/40 nm emission filters were used. The data were analyzed using SlideBook v.6.0.8 (Intelligent Imaging Innovations) and Fiji v.1.50b software.

For FRET images a 605/30 excitation filter and two emission filters (667/30 nm for miRFP670nano and 725/40 nm for miRFP718nano) were used. Emission ratios were obtained by calculating background-subtracted 605/30 and 725/40 nm image intensities divided by background-subtracted 605/30 and 667/30 nm image intensities. Images were obtained using ImageJ v.1.51u. Intensity-modulated display mode was generated with a full-spectrum lookup table. Time-course ratio measurements were normalized to baseline pre-stimulation values. Before imaging cells were starved for 6 h with DMEM medium (Gibco/Thermo-Fisher Scientific).

Photobleaching measurements were performed in live HeLa cells 48 h after the transfection using a  $\times 60$  1.35 NA oil objective lens (UPlanSApo, Olympus). Obtained raw data were normalized to corresponding absorbance spectra and extinction coefficients of the miRFPnanos, the spectrum of the Xenon lamp and the transmission of the 665/45 nm excitation filter. Photobleaching was performed using a live-cell imaging solution without antifade reagents (Invitrogen/Thermo-Fisher Scientific).

### Flow cytometry

We carried out flow cytometry analysis using an Accuri C6 flow cytometer (BD Biosciences). Before analysis, cells were washed and diluted in cold PBS to a density of 500,000 cells per ml. At least 50,000 cells per sample were recorded. The fluorescence intensity of miRFP718nano, miRFP670nano and miRFP703 and expressing cells were analyzed using the 640 nm excitation laser and 670 nm LP emission filters. EGFP fluorescence was analyzed using a 488 nm excitation laser and 510/15 nm emission filter. Supplementary Fig. 3 exemplifies the gating strategy. Flow cytometry data were collected using BD Accuri C6 v.1.0.264.21 software. The data were analyzed using FlowJo v.7.6.2 software.

### Fluorescence emission spectroscopy

Fluorescence emission spectra were acquired on an Edinburgh FLS920 fluorescence spectrometer equipped with a 450 W Xenon arc lamp (Edinburgh Xe900 450) as the excitation light source and an extended-red sensitive photomultiplier tube (Hamamatsu R2658P, spectral range 200–1,010 nm) and NIR-photomultiplier tube (Hamamatsu H10330-75, spectral range 950–1,700 nm) for detection. The excitation wavelength was set at 630 nm for miRFP703, miRFP709 and miRFP718nano, and at 580 nm for miRFP670nano.

### NIR-I and SWIR fluorescence imaging

Shown in Supplementary Fig. 9, a laboratory-made SWIR imaging system used a high-sensitivity InGaAs camera that has a broad detection

spectrum from 600 nm to 1.7  $\mu$ m (Ninox 640 II, Raptor Photonics). The camera has a pixel size of 15  $\mu$ m and a maximum frame rate of 120 Hz. The camera was equipped with a VIS-SWIR objective lens with an F-number of 1.8 (RPL-OESWIRECON14mmx1.8A, Raptor Photonics). The excitation light source was a 665 nm laser diode (M660L4, Thorlabs). The surface exciton light intensity was roughly 50 mW cm<sup>-2</sup> for all the NIR-I and SWIR imaging in this study. The camera exposure time was 10 ms for NIR-I imaging and 30 ms for SWIR imaging, if not stated otherwise. The fluorescence emission filters were 750/40 nm (FB750-40, Thorlabs) for NIR-I imaging and 1,050 nm long pass (FEL1050, Thorlabs) for SWIR imaging. A dichroic mirror with the cutoff wavelength at 730 nm (DMLP730B, Thorlabs) was used for both the NIR-I and SWIR imaging.

### Data analysis in NIR-I and SWIR imaging

The raw white-light and fluorescence images were acquired by using Micro-Manager and saved as TIFF files. Further data processing was performed using MATLAB v.2019b. The image fusion of the white-light image and the fluorescence image was done by adjusting the transparency of the fluorescence image on top of the white-light image. Before the image fusion, a threshold of three times the noise level was applied to the fluorescence images to remove the background. The signal-to-background ratio in Supplementary Fig. 14d was computed by identifying the cell regions (the 'signal') and cell-free regions (the 'background') from the white-light image. The fluorescence signal intensity in Fig. 2h was computed by averaging all the image pixels that were three times above the noise level. All the quantitative analyses with multiple animals were shown as the mean together with the individual data points.

### Animal preparation for the NIR-I and SWIR imaging

Female BALB/c mice (8–16 weeks old, 20–30 g) were used for all the NIR-I and SWIR imaging. For animal experiments, the sample size included three mice per group for each experiment. Animals were maintained on a 12 h light/dark cycle in a facility supplied with fresh air with humidity equivalent to outside ambient air. The mice were on an autofluorescence-free diet for at least 14 days before the imaging. Three days before the imaging, the abdominal region of the mice was shaved using hair-removal cream. During the imaging, the mice were anesthetized by inhaling isoflurane (1–1.5% v/v) and the body temperature was kept at 37 °C by using an electrical heating pad placed underneath. All the experimental procedures were approved by the Institutional Animal Care and Use Committee of Duke University.

### Injecting HEK293T cells into the mammary fat pad

Mice were anesthetized with 2% isoflurane in 30% oxygen balanced with nitrogen through a face mask and kept in a supine position. The fourth nipple skin was gently held up using a fine tweezer to form a tent shape, and a 27 gauge needle was inserted into the skin next to the nipple until the needle bevel was in. After 20  $\mu$ l of miRFP670nano- or miRFP718nano-expressing HEK293T cell solution was slowly injected, the tweezer was switched to hold the skin around the needle to keep the hole closed while the needle was withdrawn. Then the contralateral fourth mammary fat pad was injected using the same procedure.

### NF- $\kappa$ B-based transcription reporter of LPS-induced inflammation in mice

We followed a similar protocol adapted from ref. <sup>25</sup>. Briefly, the mice were anesthetized by inhaling isoflurane (1–1.5% v/v). Hydrodynamic injection of the NF- $\kappa$ B-miRFP718nano reporter plasmid (10%, v/wt) was performed via the tail vein. For a 20-g mouse, 2.0 ml of plasmid solution (10  $\mu$ g ml<sup>-1</sup>) was injected. The entire solution volume was injected in less than 10 s. The mice were then released to the cages for recovery. After 72 h, 100  $\mu$ l of LPS dissolved in PBS (4 mg kg<sup>-1</sup> body weight) was administered by intraperitoneal injection at the mammary gland region.

The fluorescence imaging started 12 h after the LPS administration and continued for 6.5 days.

### Reporting summary

Further information on research design is available in the Nature Portfolio Reporting Summary linked to this article.

### Data availability

The data supporting the findings of this study are available within the article and its Supplementary Information. All other data that support the findings of the study are available from the corresponding author upon request. The main plasmids constructed in this study, their maps and sequences are deposited to Addgene. For the structure of miRFP670nano: PDB ID [6MGH](https://www.rcsb.org/structure/6MGH), <https://www.rcsb.org/structure/6MGH>. For the structure of miRFP709 PDB ID: [SVIQ](https://www.rcsb.org/structure/SVIQ), <https://www.rcsb.org/structure/SVIQ>.

### Code availability

The miRFP718nano nucleotide sequence in GenBank is [MW627296.1](https://www.ncbi.nlm.nih.gov/nuccore/MW627296.1), <https://www.ncbi.nlm.nih.gov/nuccore/MW627296.1>. The miRFP-718nano structural data were deposited at the Protein Data Bank (PDB ID [7LSD](https://www.rcsb.org/structure/7LSD)), <https://www.rcsb.org/structure/7LSD>.

### References

- Otwinowski, Z. & Minor, W. Processing of X-ray diffraction data collected in oscillation mode. *Methods Enzymol.* **276**, 307–326 (1997).
- Vagin, A. & Teplyakov, A. MOLREP: an automated program for molecular replacement. *J. Appl. Crystallogr.* **30**, 1022–1025 (1997).
- Lamzin, V. S., Perrakis, A. & Wilson, K. S. in *International Tables for Crystallography, Vol. F, Crystallography of Biological Macromolecules* (eds Arnold E. et al.) 525–528 (Kluwer Academic Publishers, 2012).
- Murshudov, G. N. et al. REFMAC5 for the refinement of macromolecular crystal structures. *Acta Crystallogr. D. Biol. Crystallogr.* **67**, 355–367 (2011).
- Adams, P. D. et al. PHENIX: a comprehensive Python-based system for macromolecular structure solution. *Acta Crystallogr. D. Biol. Crystallogr.* **66**, 213–221 (2010).
- Emsley, P., Lohkamp, B., Scott, W. G. & Cowtan, K. Features and development of Coot. *Acta Crystallogr. D. Biol. Crystallogr.* **66**, 486–501 (2010).
- Longo, P. A., Kavran, J. M., Kim, M. S. & Leahy, D. J. Transient mammalian cell transfection with polyethylenimine (PEI). *Methods Enzymol.* **529**, 227–240 (2013).

### Acknowledgements

We thank N. Peitsaro and N. Aarnio from the Flow Cytometry Core Facility of the University of Helsinki for the technical assistance. This work was supported by grants from the US National Institutes of Health (NIH) (grant nos. GM122567, EB028143, NS111039 and NS115581), Chan Zuckerberg Initiative (grant no. 226178), Cancer Foundation Finland and Magnus Ehrnrooth Foundation. S.P. was supported in part by the NIH Intramural Research Program for the Vaccine Research Center of the National Institute of Allergy and Infectious Diseases.

### Author contributions

O.S.O. developed and characterized the protein in vitro and in cultured cells. C.M. developed the SWIR imaging system, performed imaging and analyzed the data. C.T. developed the SWIR imaging system and measured fluorescence emission. H.S. performed animal surgeries. S.P. designed structural biology experiments and analyzed the data. M.B. purified the recombinant proteins and prepared cells for SWIR imaging. J.Y. planned and supervised the SWIR imaging experiments and analyzed the data. V.V.V. conceived, planned and supervised the whole project and together with J.Y., O.S.O. and S.P. wrote the manuscript. All authors reviewed the manuscript.

### Competing interests

The authors declare no competing interests.

### Additional information

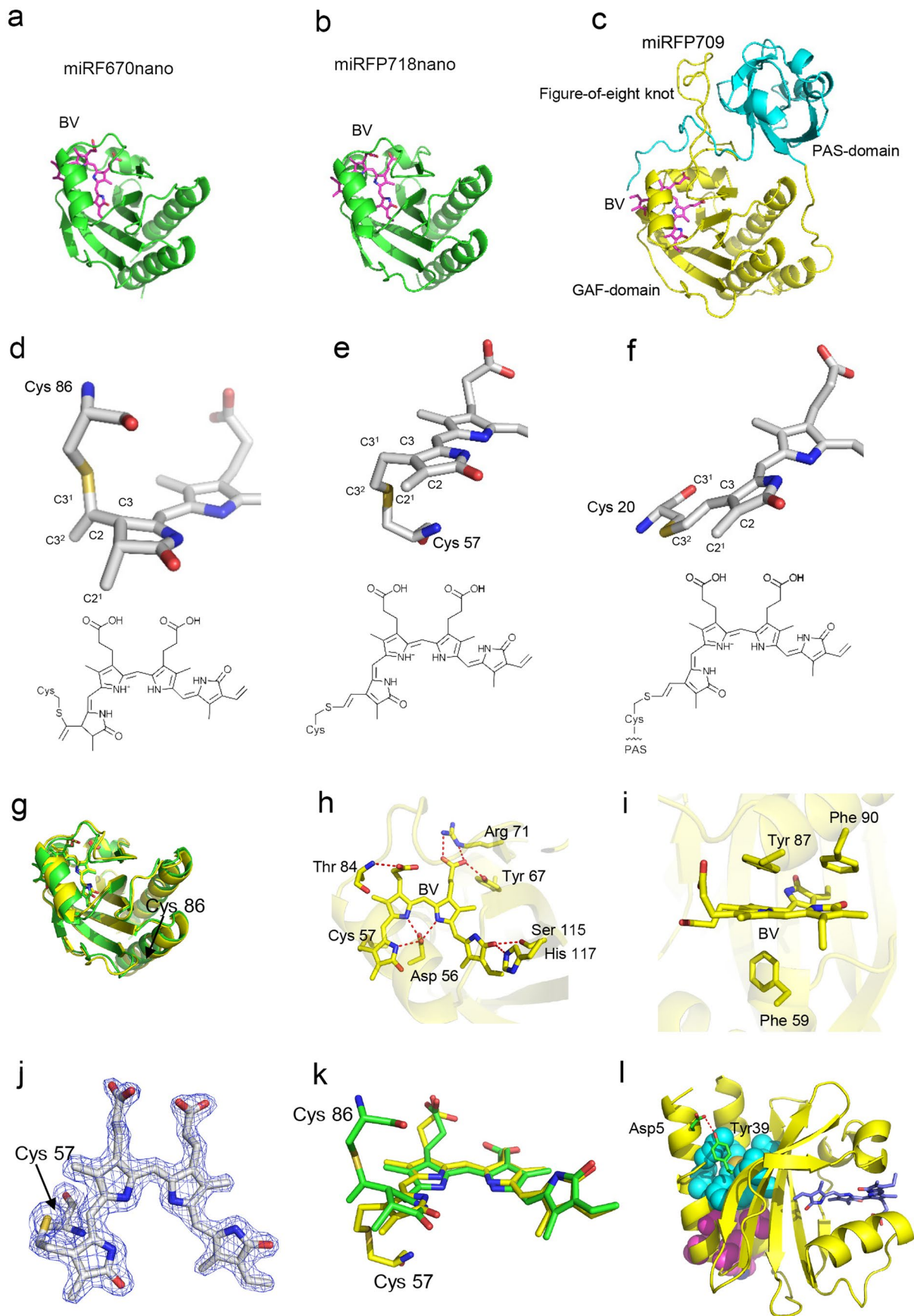
**Extended data** is available for this paper at <https://doi.org/10.1038/s41592-022-01683-0>.

**Supplementary information** The online version contains supplementary material available at <https://doi.org/10.1038/s41592-022-01683-0>.

**Correspondence and requests for materials** should be addressed to Junjie Yao or Vladislav V. Verkhusha.

**Peer review information** *Nature Methods* thanks Takeharu Nagai and the other, anonymous, reviewer(s) for their contribution to the peer review of this work. Primary Handling Editor: Rita Strack, in collaboration with the *Nature Methods* team.

**Reprints and permissions information** is available at [www.nature.com/reprints](http://www.nature.com/reprints).



Extended Data Fig. 1 | See next page for caption.

**Extended Data Fig. 1 | Structure of miRFP718nano and its red-shifted chromophore.** Overall structures of (a) miRFP670nano (PDB ID: 6MGH), (b) miRFP718nano, and (c) miRFP709 (PDB ID: 5VIQ). The biliverdin (BV) chromophores are shown in magenta. The PAS and GAF domains of miRFP709 are in cyan and yellow, respectively. The BV chromophores in (d) miRFP670nano, (e) miRFP718nano, and (f) miRFP709 bound to the respective Cys residues and their chemical formulas. Carbon, nitrogen, oxygen, and sulfur atoms are in white, blue, red, and yellow, respectively. Sticks representations show only rings A and B of the chromophores and Cys residues. In miRFP670nano, the BV chromophore (d) is bound to Cys86 via the C3<sup>1</sup> atom, miRFP718nano (e) and miRFP709 (f) have the same chromophore species bound to the Cys57 and Cys20,

respectively. (g) Superposition of miRFP670nano (green) and miRFP718nano (yellow) structures. (h) miRFP718nano hydrogen bond network around the chromophores. (i) Stacking interactions between the chromophores and the surrounding residues in miRFP718nano. (j) The chromophores of miRFP718nano bound to the respective Cys57 residues in the *2Fo-Fc* electron density map. The map is countered at 2.0 $\sigma$ -levels. (k) Superposition of the chromophores in miRFP670nano (green) and miRFP718nano (yellow). (l) Stabilizing mutations and hydrophobic clusters in miRFP718nano. The residues forming H-bonds are shown in green, hydrophobic clusters (one formed by residues Leu8, Ile11, Val12, Val26, Ile104, Leu114, Met140 and the other by Val15, Phe18, Leu19, Trp128, Phe132, Leu133) are in cyan and magenta.

## Reporting Summary

Nature Portfolio wishes to improve the reproducibility of the work that we publish. This form provides structure for consistency and transparency in reporting. For further information on Nature Portfolio policies, see our [Editorial Policies](#) and the [Editorial Policy Checklist](#).

### Statistics

For all statistical analyses, confirm that the following items are present in the figure legend, table legend, main text, or Methods section.

n/a Confirmed

- The exact sample size ( $n$ ) for each experimental group/condition, given as a discrete number and unit of measurement
- A statement on whether measurements were taken from distinct samples or whether the same sample was measured repeatedly
- The statistical test(s) used AND whether they are one- or two-sided  
*Only common tests should be described solely by name; describe more complex techniques in the Methods section.*
- A description of all covariates tested
- A description of any assumptions or corrections, such as tests of normality and adjustment for multiple comparisons
- A full description of the statistical parameters including central tendency (e.g. means) or other basic estimates (e.g. regression coefficient) AND variation (e.g. standard deviation) or associated estimates of uncertainty (e.g. confidence intervals)
- For null hypothesis testing, the test statistic (e.g.  $F$ ,  $t$ ,  $r$ ) with confidence intervals, effect sizes, degrees of freedom and  $P$  value noted  
*Give  $P$  values as exact values whenever suitable.*
- For Bayesian analysis, information on the choice of priors and Markov chain Monte Carlo settings
- For hierarchical and complex designs, identification of the appropriate level for tests and full reporting of outcomes
- Estimates of effect sizes (e.g. Cohen's  $d$ , Pearson's  $r$ ), indicating how they were calculated

*Our web collection on [statistics for biologists](#) contains articles on many of the points above.*

### Software and code

Policy information about [availability of computer code](#)

Data collection

Flow cytometry data were collected using BD Accuri C6 v.1.0.264.21. Fluorescence in cells was measured on a microscope controlled by SlideBook v.6.0.8, images were acquired by Flash4.0 V3 camera (Hamamatsu), supported by DCAM-API. X-ray data were acquired on SER-CAT 22-ID and 22-BM beamline stations (Advanced Photon Source, Argonne National Laboratory). Before data collection, the crystals were flash-frozen in a 100 K nitrogen gas stream. NIR-I and SWIR fluorescence imaging was performed by a lab-made SWIR imaging system used a high-sensitivity InGaAs camera that has a broad detection spectrum from 600 nm to 1.7  $\mu\text{m}$  (Ninox 640 II, Raptor Photonics). The camera has a pixel size of 15  $\mu\text{m}$  and a maximum frame rate of 120 Hz. The camera was equipped with a VIS-SWIR objective lens with an F-number of 1.8 (RPL-OESWIRECON14mmx1.8A, Raptor Photonics).

Data analysis

Data fitting and statistical analysis were performed using an OriginPro 2021b v.9.8.5.212 (OriginLab) and Microsoft Excel (v. 15.36) software. The Olympus IX81 microscope was operated with a SlideBook v.6.0.8 software (Intelligent Imaging Innovations). The Flow cytometry data were analyzed using a FlowJo v.7.6.2 software. FRET measurements were quantified using ImageJ v.1.51u. In vivo image data were processed in ImageJ or Fiji software (SciJava, <https://fiji.sc>). Diffraction images were processed with HKL2000. The structure was solved by the molecular replacement method with MOLREP v.11.0 using the structure of miRFP670nano (PDB ID: 6MGH) as a search model. To remove model bias, the structure was rebuilt with ARP/wARP model building and density improvement software. The structure refinement was carried out with REFMAC5 (CCP4 suite) v.8.0.005 and PHENIX.REFINE (PHENIX suite) v.1.8.4-1496 programs. A realspace model correction and structure validation were performed with COOT v.0.9.8.1. For NIR-I and SWIR imaging, the raw white-light and fluorescence images were acquired by using Micro-Manager and saved as TIFF files. Further data processing was performed using MATLAB, v. 2019b.

For manuscripts utilizing custom algorithms or software that are central to the research but not yet described in published literature, software must be made available to editors and reviewers. We strongly encourage code deposition in a community repository (e.g. GitHub). See the Nature Portfolio [guidelines for submitting code & software](#) for further information.

## Data

Policy information about [availability of data](#)

All manuscripts must include a [data availability statement](#). This statement should provide the following information, where applicable:

- Accession codes, unique identifiers, or web links for publicly available datasets
- A description of any restrictions on data availability
- For clinical datasets or third party data, please ensure that the statement adheres to our [policy](#)

Nucleotide sequence in GenBank for miRFP718nano is MW627296.1 (link: <https://www.ncbi.nlm.nih.gov/nuccore/MW627296.1>). The crystal structure for miRFP718nano in Protein Data Bank is 7LSD (link: <https://www.rcsb.org/structure/7LSD>). The data supporting the findings of this study are available within the article and its Supplementary Information. The major plasmids constructed during this research, their maps and sequences are deposited to Addgene depository. For the structure of miRFP670nano PDB ID: 6MGH; link: <https://www.rcsb.org/structure/6mgh>. For the structure of miRFP709 PDB ID: 5VIQ; link: <https://www.rcsb.org/structure/5VIQ>.

## Field-specific reporting

Please select the one below that is the best fit for your research. If you are not sure, read the appropriate sections before making your selection.

- Life sciences       Behavioural & social sciences       Ecological, evolutionary & environmental sciences

For a reference copy of the document with all sections, see [nature.com/documents/nr-reporting-summary-flat.pdf](https://www.nature.com/documents/nr-reporting-summary-flat.pdf)

## Life sciences study design

All studies must disclose on these points even when the disclosure is negative.

Sample size	Standard N>3 independent experiments were performed for most cases, unless noted in the figure legend. For flow cytometry at least 30,000 cells per sample were recorded. For animal experiments sample size included 3 mice for each experiment. Sample size was based on experience in prior studies.
Data exclusions	No data were excluded.
Replication	Usually three independent replications of the experiments were performed for all presented protein variants and labeled structures in different cells, different days of transfection and different days of recording. All attempts at replication were successful.
Randomization	Group allocation used in our study were randomly assigned to animals and cultured cells.
Blinding	Blinding is not relevant to our studies because they involved test group versus control group for evaluation performance of the constructs and the data are not relevant to clinical trials.

## Reporting for specific materials, systems and methods

We require information from authors about some types of materials, experimental systems and methods used in many studies. Here, indicate whether each material, system or method listed is relevant to your study. If you are not sure if a list item applies to your research, read the appropriate section before selecting a response.

### Materials & experimental systems

n/a	Involvement in the study
<input checked="" type="checkbox"/>	<input type="checkbox"/> Antibodies
<input type="checkbox"/>	<input checked="" type="checkbox"/> Eukaryotic cell lines
<input checked="" type="checkbox"/>	<input type="checkbox"/> Palaeontology and archaeology
<input type="checkbox"/>	<input checked="" type="checkbox"/> Animals and other organisms
<input checked="" type="checkbox"/>	<input type="checkbox"/> Human research participants
<input checked="" type="checkbox"/>	<input type="checkbox"/> Clinical data
<input checked="" type="checkbox"/>	<input type="checkbox"/> Dual use research of concern

### Methods

n/a	Involvement in the study
<input checked="" type="checkbox"/>	<input type="checkbox"/> ChIP-seq
<input type="checkbox"/>	<input checked="" type="checkbox"/> Flow cytometry
<input checked="" type="checkbox"/>	<input type="checkbox"/> MRI-based neuroimaging

## Eukaryotic cell lines

Policy information about [cell lines](#)

Cell line source(s)

HeLa (CCL-2), HEK293T (CRL-3216), NIH3T3 (CRL-1658), N2A(CCL-131) and U2OS (HTB-96) cell lines were obtained from ATCC.

Authentication	Cell lines were not additionally authenticated.
Mycoplasma contamination	Cell lines were not additionally tested for mycoplasma.
Commonly misidentified lines (See <a href="#">ICLAC</a> register)	No commonly misidentified cell lines were used.

## Animals and other organisms

Policy information about [studies involving animals](#); [ARRIVE guidelines](#) recommended for reporting animal research

Laboratory animals	Female BALB/c mice (8-16 weeks old, 20-30 g) were used for all the NIR-I and SWIR imaging. The mice were on autofluorescence-free diet for at least 14 days before the imaging. Animals were maintained on a 12 h light/dark cycle in facility supplied with fresh air with humidity equivalent to outside ambient air.
Wild animals	No wild animals were used in the study.
Field-collected samples	No field-collected samples were used in the study.
Ethics oversight	All the experimental procedures with mice were approved by the IACUC of Duke University. All the experimental procedures with rats were performed under the ethical guidelines of the European convention and regulations of the Ethics Committee for Animal Research of the University of Helsinki.

Note that full information on the approval of the study protocol must also be provided in the manuscript.

## Flow Cytometry

### Plots

Confirm that:

- The axis labels state the marker and fluorochrome used (e.g. CD4-FITC).
- The axis scales are clearly visible. Include numbers along axes only for bottom left plot of group (a 'group' is an analysis of identical markers).
- All plots are contour plots with outliers or pseudocolor plots.
- A numerical value for number of cells or percentage (with statistics) is provided.

### Methodology

Sample preparation	Prior to acquisition, cell pellets were washed with PBS and diluted in cold PBS to density 500,000 cells per ml.
Instrument	BD Accuri C6 flow cytometer.
Software	BD Accuri C6 v.1.0.264.21, FlowJo v.7.6.2.
Cell population abundance	At least 30,000 cells per sample were recorded.
Gating strategy	Initial gates - FSC-A/SSC-A to discriminate cells from debris; then cells were gated in FSC-W/FSC-A to discriminate single cells; then cells were gated in SSC-W/SSC-A to discriminate live cells. Mock transected cells were used for selecting negative population.

- Tick this box to confirm that a figure exemplifying the gating strategy is provided in the Supplementary Information.